Spatiotemporally resolved corrosion protection of AA2024-T3 by a lithium-based conversion layer

Li, Ziyu; Homborg, Axel; Visser, Peter; Gonzalez-Garcia, Yaiza; Mol, Arjan

DOI
10.1016/j.corsci.2024.112061

Publication date
2024

Document Version
Final published version

Published in
Corrosion Science

Corrosion Science 233 (2024) 112061

Contents lists available at ScienceDirect

Corrosion Science

journal homepage: www.elsevier.com/locate/corsci

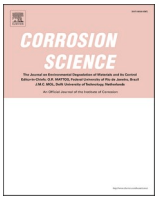

Spatiotemporally resolved corrosion protection of AA2024-T3 by a lithium-based conversion layer

Ziyu Li [a,*], Axel Homborg [a,b], Peter Visser [c], Yaiza Gonzalez-Garcia [a], Arjan Mol [a]

[a] Delft University of Technology, Department of Materials Science and Engineering, Mekelweg 2, Delft 2628CD, the Netherlands
[b] Netherlands Defence Academy, Het Nieuwe Diep 8, Den Helder 1781 AC, the Netherlands
[c] AkzoNobel, Rijksstraatweg 31, Sassenheim 2171 AJ, the Netherlands

ARTICLE INFO

Keywords:
Lithium inhibitor
SECM
Electrochemical noise
Aluminium alloy
AA2024-T3
Conversion coating

ABSTRACT

In this work, the corrosion mechanism of AA2024-T3 covered by a lithium-based conversion layer is studied with high spatial and temporal resolution. Although the aluminium alloy surface is protected by a multi-layered conversion layer, areas around intermetallic phases (IMPs) represent weak spots due to an insufficient generation of a protective inner dense layer. For the freshly formed conversion layer, both the top and the inner layer undergo a gradual dissolution upon exposure to relatively dilute NaCl solution within 2 h due to their chemical instability. For the ambiently-aged conversion layer, most corrosion activity around IMPs is related to the S-phase and large constituent phases, due to their active nature and the lower local conversion layer quality, respectively. Moreover, S-phase-related corrosion activity lasts approximately 8 h due to fast dissolution whereas reactions induced by large constituent particles remain active over the entire re-immersion period of 12 h.

1. Introduction

Aerospace aluminium alloys exhibit a high strength-to-weight ratio, favourable elastic modulus and cost-efficiency, which led to their widespread application in the aerospace industry [1–4]. However, due to their intricate microstructural heterogeneity, aerospace aluminium alloys are inherently vulnerable to localized corrosion. This necessitates the implementation of effective and active protection measures throughout their operational lifespan [5–7]. For decades, effective and reliable active protection has been achieved through the utilization of chromate-based conversion and organic coatings [8–11]. However, given its toxic and carcinogenic properties, an imperative has emerged for its substitution with chromate-free systems in response to the progressively stringent international health and safety regulations [12]. Consequently, there has been a growing focus on the advancement of alternative inhibitors that comply with current environmental, health, safety and sustainability regulations and can provide cost-effective, reliable and long-lasting corrosion protection.

In general, the exploration of chromate-free coating schemes for industrial applications can be divided into two categories: chromate-free conversion bath treatments and chromate-free organic coatings [13–16]. Based on the dominant chemical components for inhibition, these proposed strategies can be categorised into trivalent chromium [17,18], zirconium-based systems [14,19], transition metal oxyanion additives [20–22], rare earth-based compounds [23,24] and lithium salts [25–27]. Among these options studied, lithium salts have the merit of acting both as chemicals for conversion baths [28–30] and as compounds that are leachable from organic coatings [31–33]. The former was discovered in the 1980 s when Gui et al. [30] generated a Li-based conversion layer on AA6061-T6 by anodic polarization. The latter application of lithium salts was first proposed by Visser and Hayes [34] as a leaching inhibitor from organic primers and has been considered as promising for the replacement of traditional hexavalent chromate-based inhibitors [15]. The anion of lithium salts like lithium carbonate or lithium oxalate can generate an alkaline environment (pH 9–11) in a liquid environment [35], promoting the removal of the natural oxide layer, the dissolution of the aluminium matrix and finally the precipitation of a protective layer in the presence of lithium. Lithium ions play a pivotal role in the stabilization of reaction products, leading to the gradual formation of a multi-levelled and robust barrier layer [26]. This protective layer is usually of a bilayer nature, formed in a lithium-containing conversion bath. A bilayer structure including a top columnar lithium/aluminium (Li/Al) layered double hydroxide (LDH) layer and an inner dense lithium-containing pseudoboehmite

* Corresponding author.
E-mail address: Z.Li-12@tudelft.nl (Z. Li).

https://doi.org/10.1016/j.corsci.2024.112061
Received 23 February 2024; Received in revised form 6 April 2024; Accepted 15 April 2024
Available online 16 April 2024

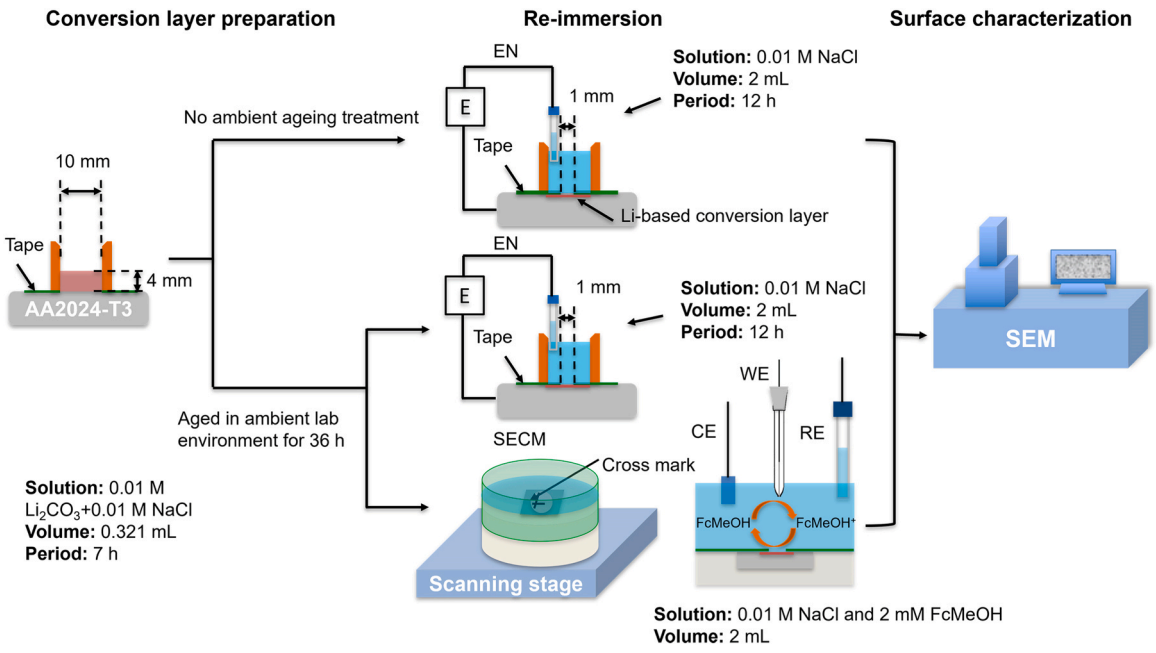

Fig. 1. Schematic overview of the experimental procedure.

(Li-pseudoboehmite) layer forms on the aluminium matrix.

In contrast, only a columnar layer is observed over IMPs (S-, θ- and constituent phases) [36]. At coating defect areas of lithium leaching organic coatings, a bilayer or triple layer (including an extra middle porous sublayer) configuration is typically formed since the local chemistry and pH from a leaching system are much more complex and dynamic [32,36]. Li et al. have presented a detailed summary of the protective layer formation mechanism in a recent review [37].

Various alloying elements and thermomechanical processing treatments contribute to a highly heterogeneous microstructure and the formation of intermetallic phases/particles (IMPs) in the bulk and at the surface of aluminium alloys [1]. The presence of IMPs significantly influences the conversion layer growth at and around IMPs at the aluminium alloy surface due to the distinct chemical interaction between the IMPs and the adjacent aluminium matrix [38,39]. Waldrop et al. [39] observed that the nucleation rate during the chromate conversion coating (CCC) on AA2024-T3 was different on various types of IMPs: the growth rate at IMPs with higher copper content was lower. Campestrini et al. [8,40] reported the negative effect of IMPs on the corrosion protection of CCC for AA2024-T3 due to the formation of large defects near IMPs. Šekularac et al. [41] studied zirconium conversion coating formation and the corrosion resistance on aluminium alloys of series 1xxx up to 7xxx. The results showed that copper rich-IMPs in AA2024-T3 were detrimental to the generation of a uniform conversion layer. The conversion layer was significantly thicker at Cu-rich IMPs than that over the matrix. For the case of AA7075-T6, although a uniform conversion layer was produced, zinc-rich areas were highly vulnerable to pitting corrosion when exposed to a NaCl solution. Up to now, already a proper understanding of the structure, morphology and composition of the lithium-based conversion layer on AA2024-T3 has been achieved [36,42]. In addition, our previous work has reported multiple types of experiments to evaluate the corrosion protective behaviour of a lithium-based conversion layer using traditional accelerated exposure and electrochemical characterization including salt spray testing, potentiodynamic polarization and electrochemical impedance spectroscopy (EIS) [43–45]. However, a detailed investigation at the microscale of the corrosion mechanism of lithium-based conversion coated AA2024-T3 is still missing. A profound understanding of the corrosion mechanism at the level of IMPs is of pivotal importance to optimize the lithium-based conversion process and its further development towards a sustainable green corrosion protection technology.

Although IMPs in aerospace aluminium alloys contribute significantly to the improvement of their mechanical properties due to the generation of a heterogeneous microstructure, the same heterogeneity also governs a reduced local corrosion resistance of these alloys [5–7]. Therefore, it is of pivotal importance to investigate the mechanistic role of IMPs in local corrosion protection within corrosion inhibition strategies. This study is devoted to elucidating the corrosion mechanism of a lithium-based conversion coated AA2024-T3 at both IMPs and the aluminium matrix at high spatial and temporal resolution. Top-view and cross-sectional micrographs were obtained by focused ion beam-scanning electron microscopy (FIB-SEM) to compare the morphological and compositional variation before and after exposure to a corrosive NaCl solution. Electrochemical noise (EN) analysis was adopted to monitor the electrochemical signature resulting from localized corrosion in real time during exposure. Unlike traditional EIS which records electrochemical information at several discrete time points, the EN technique enables continuous and time-resolved monitoring of electrochemical reactions without external perturbation. This capacity is of vital importance in identifying relatively rapid electrochemical reactions such as those related to localized corrosion events. Scanning electrochemical microscopy (SECM) technique in feedback operation mode was applied to study the localized corrosion with high spatial resolution.

2. Material and methods

2.1. Materials and experimental set-up

All the material used in this work originated from a single commercial AA2024-T3 sheet acquired from Goodfellow, with a thickness of 0.8 mm. Square specimens measuring 20 mm × 20 mm were fabricated from the aforementioned sheet. All specimens were ground up to grit 4000 SiC abrasive paper, then underwent subsequent gentle cleaning with distilled water, drying through compressed air and were subsequently left in an ambient laboratory environment for 24 hours preceding the experiments. For all samples, water-proof tape was used to cover the surfaces with a circular opening of 10 mm in diameter to affix and restrict the exposed surface area. Laboratory-grade chemicals used

in this work were ordered from Sigma-Aldrich (St. Louis, MO, USA).

The detailed experimental procedure is shown in Fig. 1. The lithium-based conversion layer was firstly fabricated in a 0.01 M NaCl and 0.01 M Li_2CO_3 (pH 10.9) solution for an immersion duration of 7 h. This immersion duration was selected in order to be consistent with a previous work and to allow a relatively mature lithium-based conversion layer to be formed [36]. An electrolyte layer of 4 mm in height, equivalent to a volume of 0.321 mL at a diameter of a circular exposed surface of 10 mm, was established in the experimental sets to replicate the specific liquid environment within a 1 mm width artificial defect inside an organic coating loaded with lithium inhibitors [42]. The prepared conversion coatings were divided into two groups: (i) the freshly formed lithium-based conversion layer was evaluated using EN measurements and SEM whereas (ii) the 36 h ambiently-aged samples were studied using EN, SEM and SECM. Ambiently-aged samples were adopted here to reduce the interference of the dissolution of the freshly formed conversion layer with subsequent SECM measurements. Before subsequent re-immersion measurements, both types of samples were gently cleaned with distilled water and dried with cold compressed air. For re-immersion tests, the exposed surface was 1 mm in diameter, with the addition of 2 mL 0.01 M NaCl. For SECM measurements, 2 mM FcMeOH was added as the redox mediator. The exposed areas were examined using optical microscopy in order to guarantee the absence of visually large defects. The two types of the lithium-based conversion layers were measured by EN for a duration of 12 h. After re-immersion, samples were gently washed with distilled water and subsequently observed using the SEM. All experiments were performed under open-to-air conditions.

2.2. Focused ion beam-scanning electron microscopy (FIB-SEM) characterization

In order to study the degradation of the lithium-based conversion layer as a function of exposure time, a series of cross-sectioning measurements were performed using a FIB-SEM (Helios G4 PFIB UXe, Thermo Fisher Scientific, USA) equipped with a xenon plasma focused ion beam (PFIB), employing an accelerating voltage of 30 kV. The top-view and cross-sectional SEM characterizations were conducted at 20 keV collecting emitted secondary electrons (SE) in ultra-high-resolution mode. The chemical composition of distinct regions was assessed through Energy Dispersive Spectroscopy (EDS). It is noteworthy that, in order to mitigate the risk of potential damage to the lithium-based conversion layer, a protective Pt or C overlay coating was deposited before milling.

2.3. Electrochemical noise (EN) measurements and analysis

For the EN experiments, a two-electrode configuration was used in this work. Therefore, only potential signals were monitored. Electrical connection was established using a Cu tape connected to the working electrode. The reference electrode (RE) used for EN was an Ag/AgCl, saturated KCl electrode and all potential values presented are with

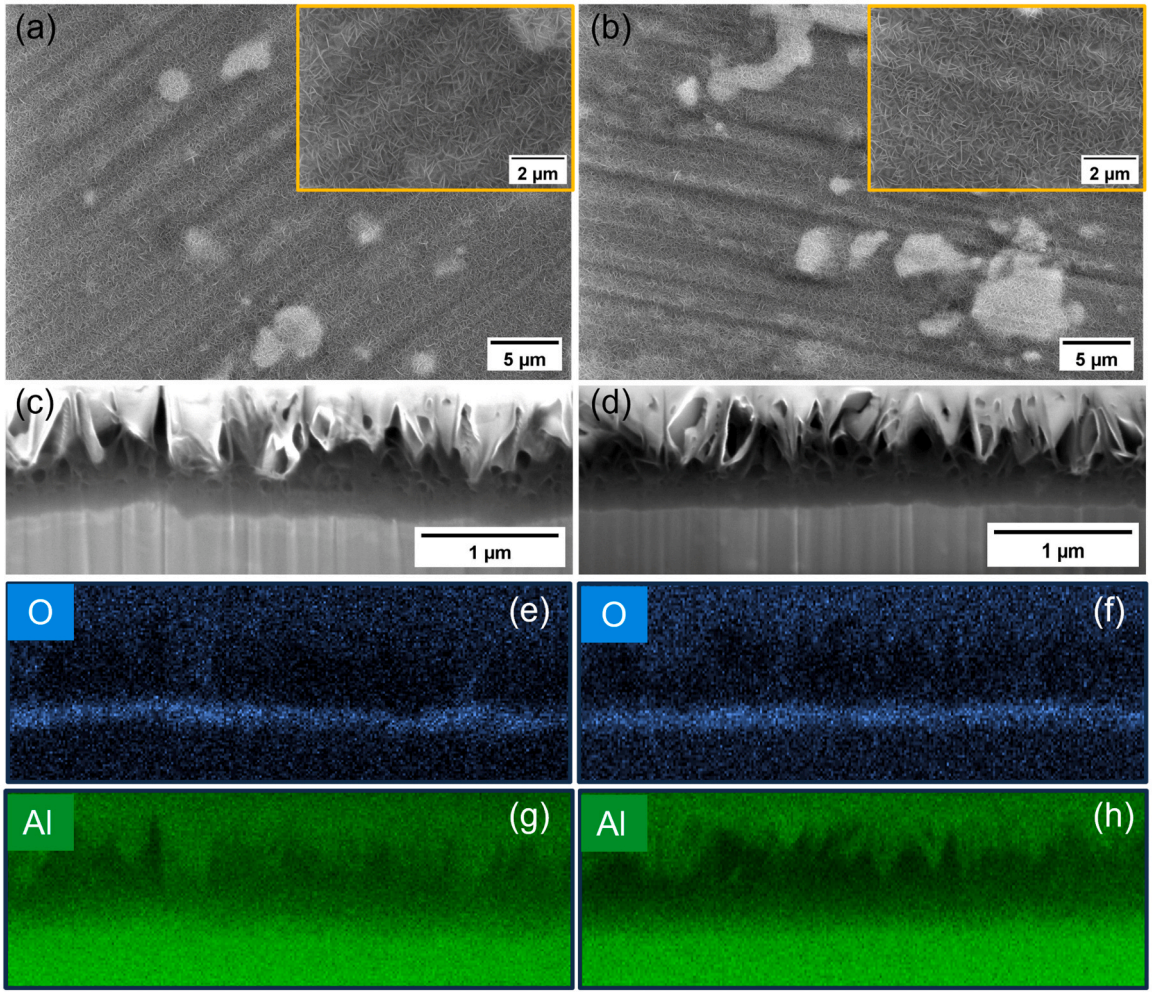

Fig. 2. (a, b) Top view, (c, d) cross-sectional view and corresponding EDS mapping of the element (e, f) oxygen and (g, h) aluminium of the lithium-based conversion layer after 0 h and 36 h ambient ageing, respectively.

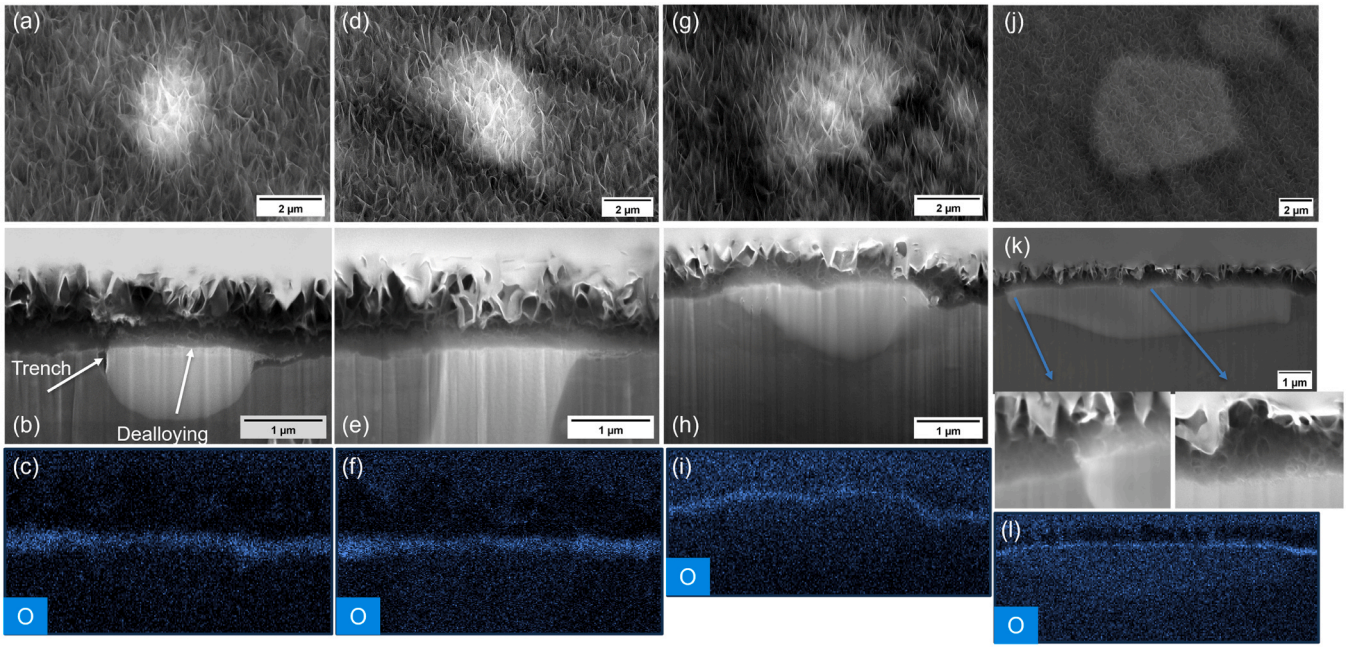

Fig. 3. Top view, cross-sectional view and corresponding oxygen distribution for the (a-c) S-phase, (d-f) θ-phase, (g-i) small constituent particle and (j-l) large constituent particle, respectively.

respect to this reference unless stated differently. All EN measurements were conducted under open-circuit potential (OCP) conditions. A Compactstat (Ivium Technologies) was used to record the potential signals. A Faradaic cage was utilized to position the Compactstat as well as the electrochemical cell, thereby mitigating potential interference from external electromagnetic sources. The sampling frequency was set at 20 Hz and a low-pass filter of 10 Hz was used to avoid aliasing. The EN data were analysed using Matlab from MathWorks. All EN measurements were performed at least in triplicate. In the EN potential signal, a DC component becomes unavoidable owing to the nonlinear and non-stationary corrosion system. The DC drift is reflected from the varying mean OCP value. The DC component, devoid of meaningful information, introduces false low frequencies and poses a potential interference in signal processing [46,47]. Consequently, effective removal of the DC trend is necessary, while concurrently preserving pertinent data to the greatest extent before subsequent analysis. Prior investigations have suggested different strategies for trend removal, like moving average, polynomial and linear trend removal, wavelet analysis and empirical mode decomposition [46,47]. In this work, a time-frequency trend removal was adopted using empirical mode decomposition (EMD), after which the signal was analysed using the Hilbert–Huang transform (HHT). EMD is a data analysis technique used in signal processing, which is particularly useful for analysing non-linear and non-stationary signals [48]. The fundamental concept of EMD indicates that a given signal can be dissected into a series of Intrinsic Mode Functions (IMFs). These IMFs are elemental constituents expressing distinct frequency bands inherent to the process under investigation. The decomposition procedure involves the repeated extraction of IMFs through a sifting process, leaving behind a residue after each iteration [49]. The sifting process stops automatically when the residue becomes less than a predefined threshold value of significance, or when it manifests as a single oscillation [50]. EMD precedes HHT: the HHT is applied to each IMF component to obtain instantaneous frequencies and amplitudes at any moment in time [50]. All the amplitudes shown in this work are relative amplitudes of the instantaneous frequencies in the spectrum.

2.4. SECM instrumentation and experimental procedures

SECM was executed using Biologic Instruments SECM model M370. A Pt disk ultramicroelectrode (UME), 10 μm in diameter, with an RG (defined as the radius of the insulating glass sheath divided by the radius of the platinum disk) of 5, was purchased from CH Instruments Inc. and was employed as a working electrode. An Ag/AgCl, saturated KCl and a Pt thin plate were used as RE and counter electrode (CE), respectively. For SECM samples, a cross mark was made before the generation of the lithium-based conversion layer to locate the scanned area during SEM observations. Demonstrating exceptional spatial resolution and electrochemical sensing capabilities, SECM proves powerful for characterizing both morphology and the presence of redox reactions at the metal/electrolyte interface [51]. SECM not only provides insights into reaction mechanisms but also facilitates the evaluation of surface reactivity across heterogeneous surface phases [52]. Please note that in this study further specification and distinction of closely positioned anodic and cathodic sites is limited due to the similarity in dimensions of the UME and the microstructural heterogeneities studied. Its application has been widespread in corrosion-related investigations, such as studies on pitting [53,54] and inhibition [55,56]. In this work, the feedback mode was utilized based on the redox mediator FcMeOH. Cyclic voltammetry (CV) was performed to verify the cleanliness of the SECM probe, locating the probe several millimetres above the surface before any SECM measurement. All current signals were normalized using the steady-state current from the CV measurements. The stage was levelled by measuring at least three negative feedback approach curves (not in the same straight line). The levelling and localization of the mark took approximately 30 min before formal SECM mapping. The distance between the tip and the substrate was around 5 μm using a negative feedback curve over the conversion layer. Mapping was performed repeatedly over the same working area of 200 μm × 150 μm with a scanning speed of 10 μm/s, increment steps of 5 μm and waiting time of 0.1 s at each point. The UME was biased at a voltage of 0.5 V to oxidize FcMeOH while the substrate was kept at an OCP state. All experiments were performed under ambient lab conditions, in a solution open to air. Experiments were triplicated to validate reproducibility.

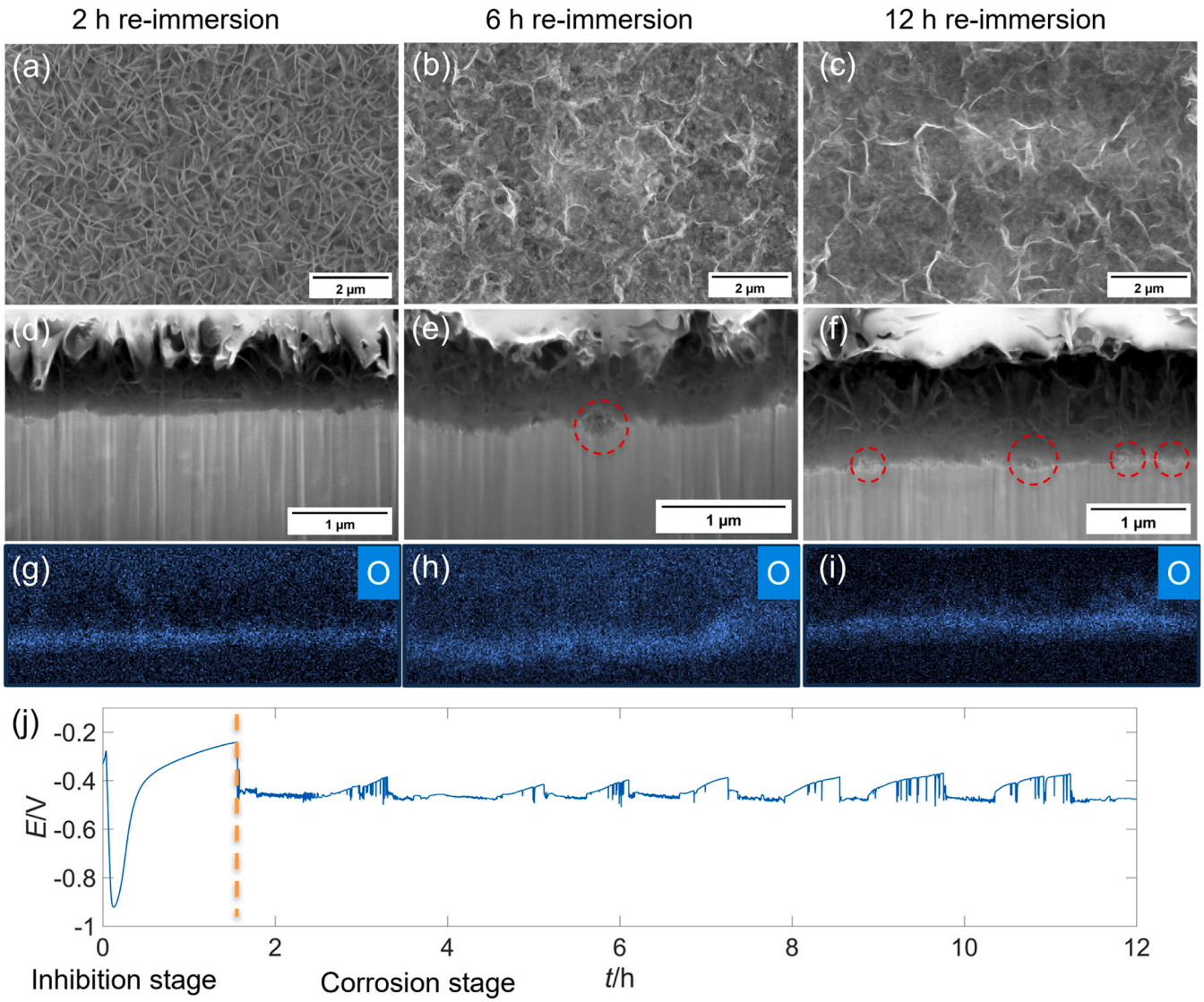

Fig. 4. Top view of the freshly formed lithium-based conversion layer after re-immersion for a duration of (a) 2 h, (b) 6 h, (c) 12 h; cross-sectional view of the freshly formed conversion layer after re-immersion for (d) 2 h, (e) 6 h, (f) 12 h and (g) corresponding oxygen distribution of 2 h, (h) 6 h, (i) 12 h. (j) EN potential signal during re-immersion for 2 h in a 0.01 M NaCl solution.

3. Results and discussion

3.1. SEM characterisation of the conversion layers before re-immersion

Fig. 2 shows the top-view and cross-sectional view of the freshly formed and 36 h ambiently-aged lithium-based conversion layer and cross-sectional EDS mapping (aluminium and oxygen) at the aluminium matrix. There is no visible difference in morphology between the differently aged samples (Figs. 2**a** and 2**b**). This observation is in contrast to the results reported previously [57] since the sample surface was dried by compressed air in this work whereas the conversion layer studied before was kept wet. Therefore, the continuous growth of the lithium-based conversion layer was hindered due to the loss of water [57]. Fig. 2**c** and Fig. 2**d** present the cross-sectional views of 0 h and 36 h aged conversion layers, respectively. A bilayer structure is present including a top columnar layer and an inner dense layer [36,42]. Hence, the ambient ageing process does not seem to affect this dual-layer structure. EDS characterization shown in Figs. 2**e**-2**h** presents the elemental distribution of aluminium and oxygen. It is clear that the inner layer is relatively oxygen-rich, which corresponds well with previous reports [58,59].

The conversion layer morphological characterization over the IMPs was considered necessary since IMPs exhibit distinct electrochemical properties as compared to the surrounding aluminium matrix and may therefore result in different conversion layer configurations. In this work, three types of IMPs, involving S-, θ- and constituent phases, are investigated. In Fig. 3, the top-view, cross-sectional view and oxygen distribution are listed, respectively. The EDS characterization of the listed IMPs is shown in Fig. S1. Fig. 3**a-c** present the case for the S-phase. From the top view, the top columnar layer uniformly covers the surface at and around the S-phase (Fig. 3**a**). A detailed chemical conversion layer structure is presented in Fig. 3**b**. Unlike the bilayer configuration formed over the aluminium matrix, the conversion layer on the S-phase mainly consists of a single columnar layer, accompanied by an incomplete inner dense layer. In addition, obvious trenching and dealloying are observed due to the high chemical instability of the S-phase [60]. The presence of this inner layer can be confirmed by the faint oxygen-rich layer in Fig. 3**c**. A similar phenomenon is also observed in the θ-phase (Fig. 3**d-f**) as well. For the case of the constituent particles, two types of cases are revealed here: small (< 2 μm) and large (> 4 μm) constituent phases. As shown in Fig. 3**g-i**, the morphology and oxygen distribution for small constituent particles are similar to conversion

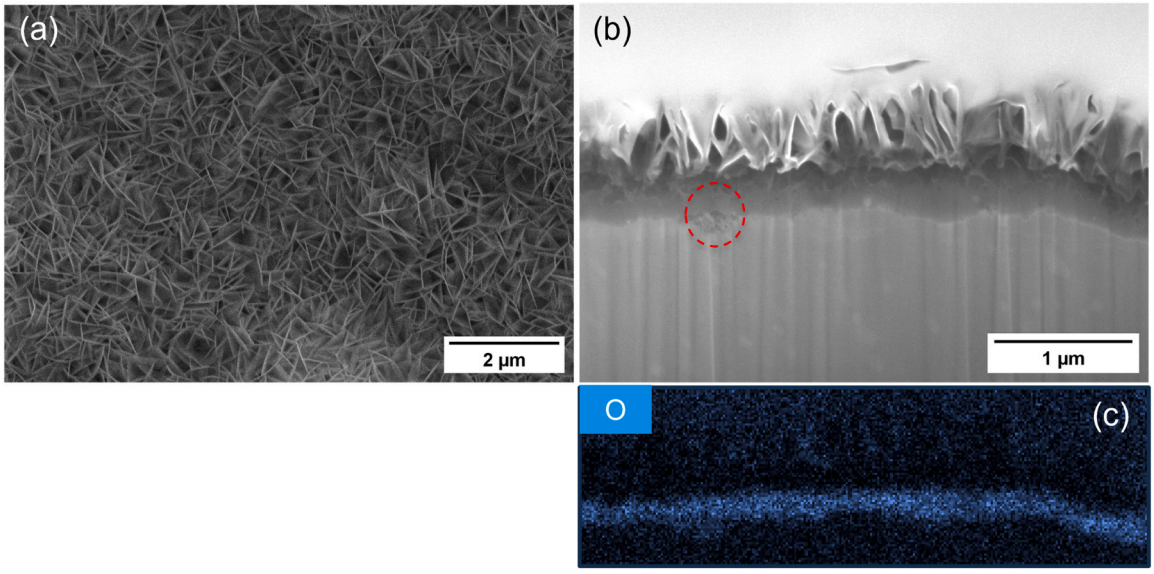

Fig. 5. (a) Top view, (b) cross-sectional view and (c) corresponding oxygen distribution mapping of the 36 h ambiently-aged lithium-based conversion layer after 12 h re-immersion in a 0.01 M NaCl solution. The dashed circle indicates localized corrosion underneath the conversion layer.

layer structure features over the S- and θ-phase. However, for the situation of the large constituent phase (Fig. 3**j-l**), the columnar layer still uniformly covers the entire top face but the incomplete inner layer is nearly indistinguishable, which is indicated by the relatively low brightness of the oxygen mapping over the particle (Fig. 3**l**). The zoomed-in figures of the large constituent phase indicate that only the columnar structure is formed. According to previous studies by Kosari et al. [36], the dual layer structure of the lithium-based conversion layer only appears on the aluminium matrix while a single columnar layer forms on the S-, θ-, and constituent phases. The absence of the inner layer over the IMPs is possibly related to the insufficient supply of aluminium, since aluminium is one of the constituent elements distributed over the entire lithium-based conversion layer [58,59]. The chemically unstable S-phase endures a relatively fast dealloying (mainly magnesium and aluminium) when the aluminium alloy surface is exposed to the aggressive electrolyte [36,38,60] and the dissolved aluminium promotes the top columnar layer formation, even preceding that over the adjacent aluminium matrix [36]. However, the conversion layer growth over more electrochemically stable θ-, and constituent phases is slower than this process over the aluminium matrix, and the supply of aluminium relies on the lateral diffusion of dissolved aluminate ions to generate the columnar layer. The absence of the incomplete inner layer over IMPs in the work of Kosari et al. [36] may be attributed to the different experimental configurations used in that work. Although the ratio of the exposed surface to the volume of electrolyte, the composition of the conversion solution and the immersion duration are identical, the exposed surface in this work is only one-quarter of the size implemented by Kosari et al. [36]. Therefore, the generation of the incomplete inner dense layer observed in this work is expected to stem from the lateral diffusion of aluminate ions during the conversion layer formation. Considering that the inner layer is formed below the top columnar layer and also its relatively low growth rate [36,58], for the small particles, the lateral propagation can fully cover the entire surface whereas the large constituent particles cannot be reached within the time of immersion, due to their larger size and larger electrochemical stability. More evidence to support this explanation is the fact that an obvious and complete inner layer was observed over a copper-rich intermetallic particle at a coating defect area of a lithium-leaching organic coating system after exposure to a relatively long 168 h neutral salt spray test [61].

3.2. SEM characterization of the conversion layers after re-immersion

Previous work has focused on the re-immersion behaviour of the lithium-based conversion layer by exposing the freshly formed or ambiently-aged conversion layer to a lithium-free NaCl solution [57,62]. However, these studies mainly focused on electrochemical characterization, which was insufficient to understand the degradation mechanism in relation to specific microstructural heterogeneities. Here, morphological characterization combined with EDS analysis is adopted to elucidate the laterally resolved degradation mechanism of the lithium-based conversion coated AA2024-T3 substrate.

For the freshly formed conversion layer, Fig. 4 shows the top-view, cross-sectional view and oxygen distribution of the aluminium matrix after re-immersion in a lithium-free NaCl solution for 2 h, 6 h, 12 h and the corresponding EN potential signal, respectively. From Fig. 4**a-c**, it is clear that the top columnar layer undergoes a gradual decomposition. This instability might be attributed to the reversible intercalation process of the Li/Al LDH top layer [63]. For instance, the de-intercalation process of lithium ions proceeds when a freshly formed Li/Al LDH is exposed to a Li-free solution [64]. This phenomenon was not observed previously [57,62] since the solution volume used in previous work is much smaller than that applied here (0.321 ml vs. 2 ml respectively). The rapid increase of the concentration of lithium ions in a small volume of solution gradually hinders a further de-intercalation of Li/Al LDH. Fig. 4**d-f** present the cross-sectional view of the lithium-based conversion layer. Although the bilayer structure is still visible during the 12 h re-immersion, the corrosion attack indicated by the red circles is clearly observable and the number of corrosion sites gradually increases with the re-immersion duration. This can be attributed to corrosive chloride ions penetrating the conversion layer at certain specific sites. Fig. 4**g-i** show the corresponding oxygen mapping of Fig. 4**d-f**: the gradual drop of the intensity of oxygen in Fig. 4**g** (2 h re-immersion) and **4 h** (6 h re-immersion) reveals that the inner layer suffers from damage as well. It was presented that the inner dense layer can release lithium carbonate during re-immersion as well [57], therefore the decreased oxygen intensity might be related to the loss of lithium carbonate from Li-pseudoboehmite. The increased oxygen brightness shown in Fig. 4**i** may be caused by the thickening of oxide or hydroxide corrosion products after 12 h re-immersion. Fig. 4**j** shows the EN potential signal during re-immersion for the freshly formed conversion layer. Identical to our previous finding [57], the entire process can be divided into two

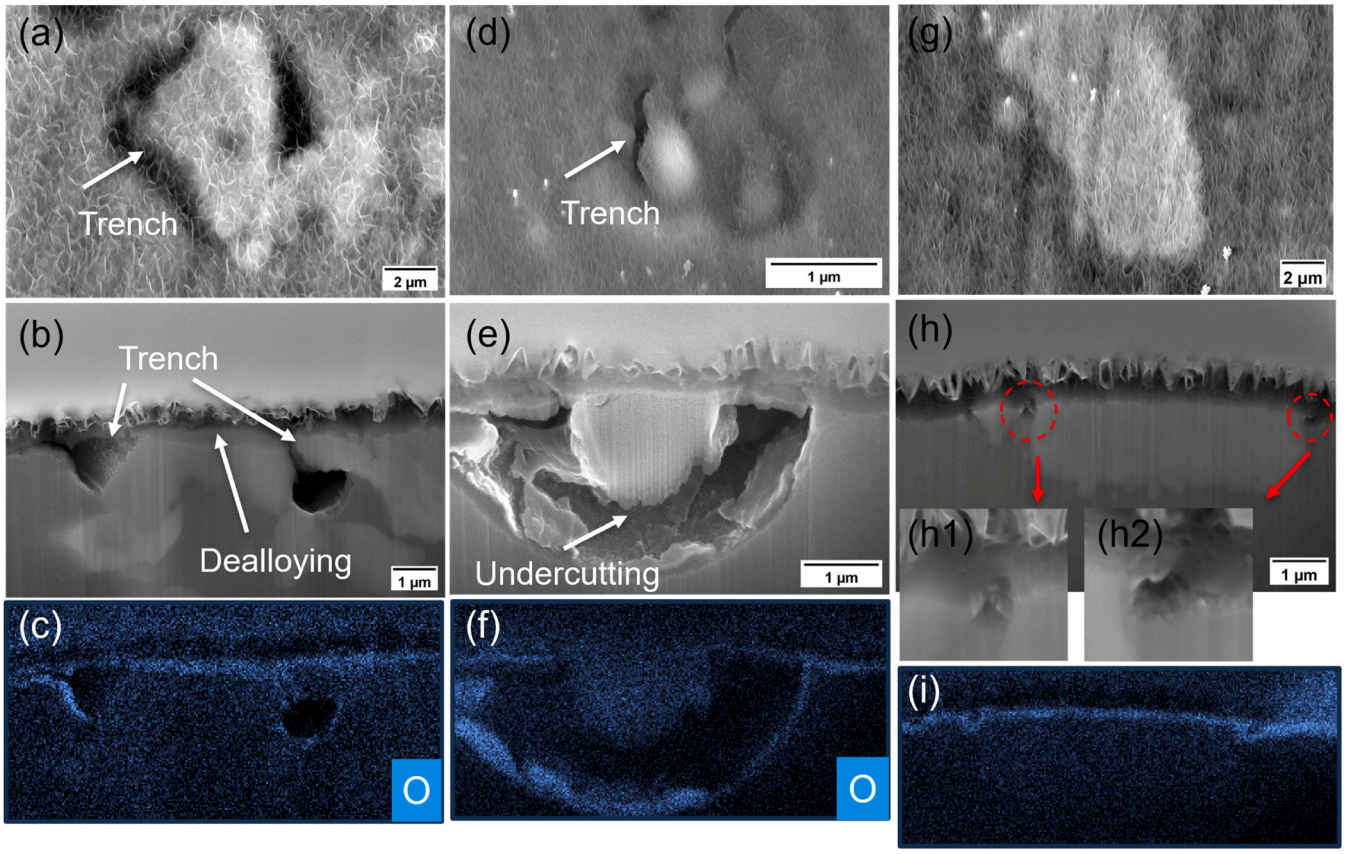

Fig. 6. (a) Top view, (b) cross-sectional characterization and (c) corresponding oxygen mapping for a constituent particle with trench from the 36 h ambiently-aged lithium-based conversion layer after 12 h re-immersion in a 0.01 M NaCl solution; (d) top view, (e) cross-sectional characterization and (f) corresponding oxygen mapping for a S-phase with trench from the aged lithium-based conversion layer after 12 h re-immersion; (g) cross-sectional view of a constituent phase at the early stage of trench formation, with (g1) and (g2) cut-outs indicated by the red dashed circles and (i) its corresponding oxygen mapping.

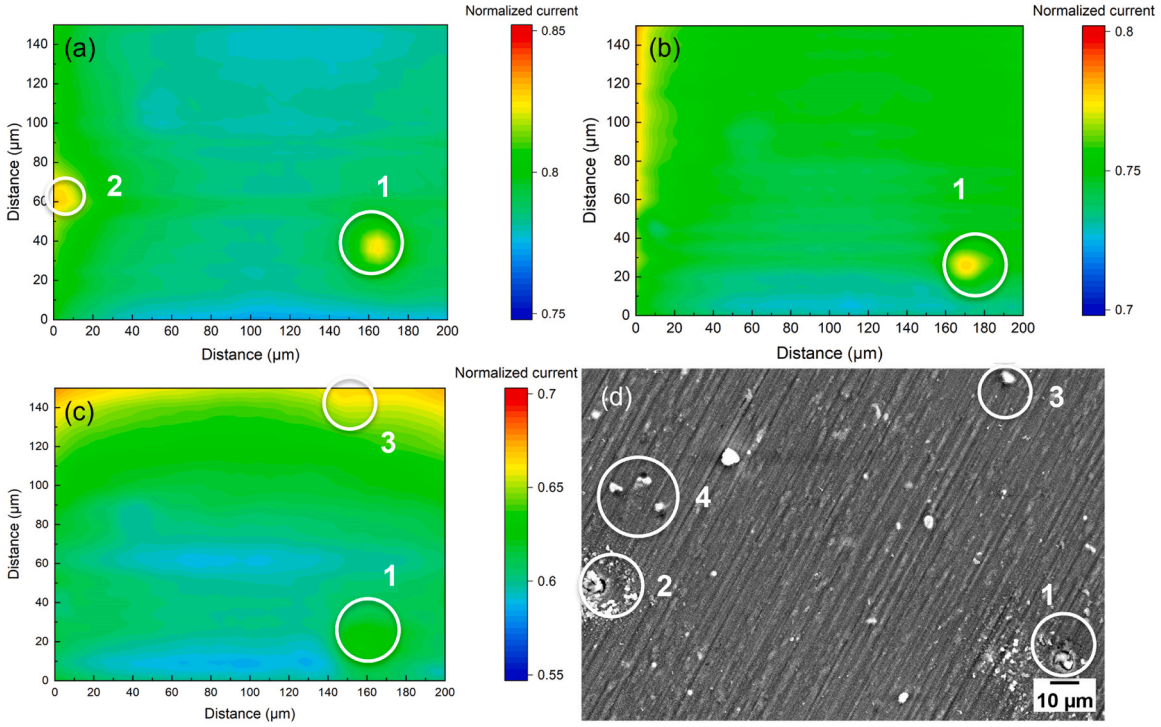

Fig. 7. SECM mapping of a fixed scanning area over a 36 h ambiently-aged lithium-based conversion layer during re-immersion in a 0.01 M NaCl electrolyte containing 2 mM FcMeOH. The scanning time duration is (a) 0.5–1.5 h, (b) 4.5–5.5 h, (c) 8.5–9.5 h. (d) Corresponding SEM micrograph.

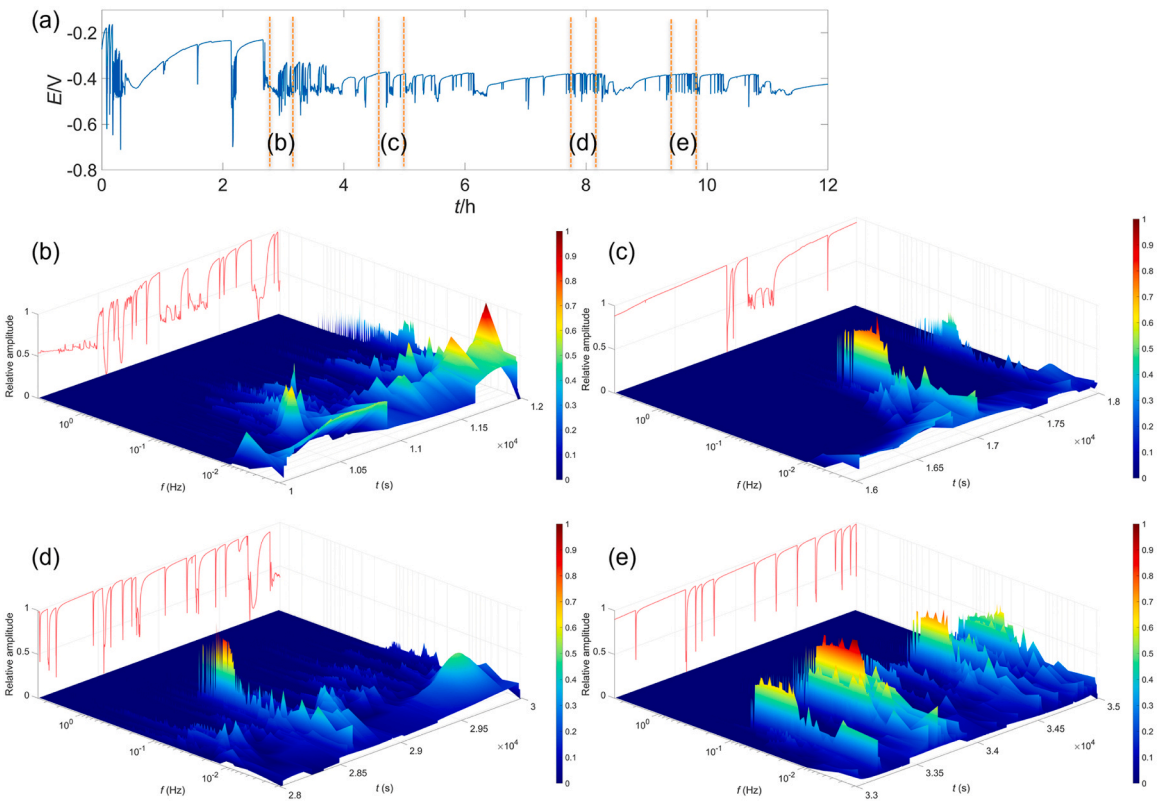

Fig. 8. EN potential signal for the 36 h ambiently-aged lithium-based conversion layer exposed to a 0.01 M NaCl solution for a duration of 12 h (a), Hilbert spectrum of the potential signal of a 36 h ambiently-aged lithium-based conversion layer exposed in a 0.01 M NaCl solution in the timeframe of (b) 10000–12000 s, (c) 16000–18000 s, (d) 28000–30000 s and (e) 33000–35000 s. The dashed lines in Fig. 6.8a correspond to the selected timeframes from Fig. 6.8b to 6.8e.

stages: the inhibition stage and the corrosion stage. The release of trapped lithium ions contributes to the appearance of the inhibition stage, and this stage gradually ends when the local concentration of lithium ions is below the minimum concentration for effective inhibition [57]. Trenches surrounding IMPs are also observed, but considering that the corrosion mechanism is nearly identical to that over the aged lithium-based conversion layer, a detailed description and explanation of the trench formation will be presented later in Section 3.5. On the contrary, as shown in Fig. 5, the top-view characterization of the 36 h ambiently-aged lithium-based conversion layer after 12 h re-immersion (Fig. 5**a**) shows little difference as compared to Fig. 2**b**. This observation is consistent with the previous finding that ambient ageing is beneficial for the stabilization of the lithium-based conversion layer [57]. Fig. 5**b** and Fig. 5**c** exhibit the cross-sectional imaging and corresponding oxygen distribution, respectively. It is clear that fewer corrosion sites have originated as compared to that in Fig. 4**f** and the oxygen-rich layer is still relatively intact, which indicates enhanced corrosion resistance properties.

The corrosion morphology and oxygen mapping at and around IMPs is presented in Fig. 6. Among the studied specimens, trenches around the S-phase and large constituent particles are mostly observed. The EDS mapping of IMPs shown in Fig. 6 is presented in Fig. S2. Fig. 6**a-c** and Fig. 6**d-f** present the top view, cross-sectional view and corresponding oxygen distribution of a constituent particle and a S-phase, respectively. Although the top columnar structure is relatively intact close to the IMP, the corrosion attack already penetrates deep underneath the conversion layer at the area in contact with the IMP. This result indicates that areas adjacent to IMPs are more prone to corrosion attack since the inner dense layer is not fully matured over the IMPs. A partial dealloying is seen in the top region of the constituent phase (Fig. 6**b**), whereas the S-phase (Fig. 6**e**) is totally dealloyed due to its higher electrochemical activity and smaller size [60]. Oxygen-rich zones (Figs. 6**c** and 6**f**) underneath the conversion layer are mainly located at the aluminium matrix side (corrosion products), which indicates that the aluminium matrix serves as the anodic region. At the same time, IMPs, gaining nobility with dealloying, act as cathodic zones until the final detachment of IMPs from the aluminium matrix. Moreover, the corrosion products shown in Fig. 6**e** are thicker as compared to those of Fig. 6**b**, suggesting that the galvanic interaction between the matrix and the S-phase is stronger than that of the galvanic couple between the matrix and the constituent particle. Figs. 6**g** and 6**h** show the top view and cross-sectional view of a large constituent phase at its early corrosion stage, with the cut-out figures of the red dashed circles presented in Figs. 6**h1** and **6h2**, respectively. This observation clearly shows that the trench initiates from the edges of the IMPs, although any initial indication from the top-view is lacking. The oxygen distribution at the trench (Fig. 6**i**) shows that the edge of the constituent particle and the adjacent aluminium matrix underneath the conversion layer are both covered with an oxygen-rich layer, indicating the dealloying zone and aluminium hydroxide, respectively.

3.3. SECM characterization

SECM mapping was performed at a fixed location to monitor the localized corrosion activities over time. SECM imaging of the immersion periods from 0.5–1.5 h, 4.5–5.5 h and 8.5–9.5 h is shown in Fig. 7**a**, **b**, and **c**, respectively. The matched SEM figure is presented in Fig. 7**d** and its corresponding EDS mapping results are listed in Fig. S3. Initially, two active sites are detected (marked with numbers 1 and 2), corresponding to the location of two constituent phases in Fig. 7**d**. This finding corresponds well with the results above those constituent particles, especially those with relatively large size, are more vulnerable to corrosion during re-immersion. With a re-immersion duration of 4.5–5.5 h, the two constituent phases remain active but at a lower reactivity. This may be

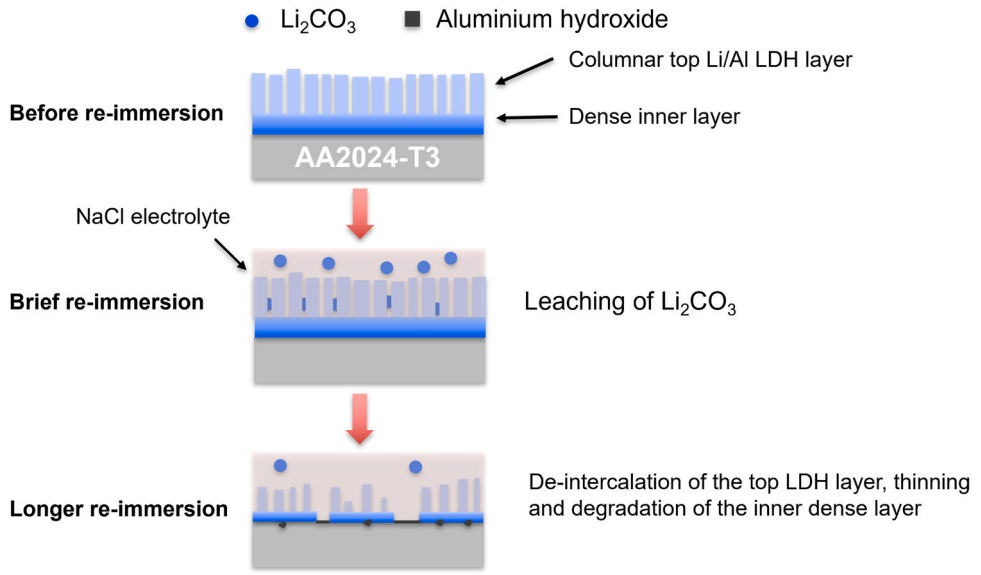

Fig. 9. Schematic representation of the proposed corrosion mechanism at the aluminium matrix of the freshly formed lithium-based conversion layer during re-immersion.

caused by the in-depth penetration of the corrosion front, which hinders the outward diffusion of FcMeOH and the generation of corrosion products which partially cover the active surface. At continued re-immersion (8.5–9.5 h), the region at constituent phase 2 is almost passive and phase 1 still exhibits a very low reactivity. In addition, another active site is observed at the top of Fig. 7**c** (marked with 3), again corresponding with the location of a constituent particle. The corrosion related to the S-phase is marked with number 4 but their signal remains undetected by the SECM tip, which may result from the limitation of the tip resolution or the relatively fast corrosion kinetics since one complete surface area mapping takes almost 1 h. The SECM characterization corroborates the findings reported earlier that S-phases and large constituent particles are the weak spots in the lithium-based conversion layer. In addition, the active state of a constituent particle can last for several hours.

3.4. EN analysis for the ambiently-aged conversion layer

Fig. 8 presents the potential variation of the 36 h ambiently-aged conversion layer under re-immersion conditions for a duration of 12 h in a NaCl solution and the Hilbert spectrum analysis for the timeframes of 10000–12000 s, 16000–18000 s, 28000–30000 s, 33000–35000 s, respectively. Unlike the freshly formed conversion layer, the inhibition stage is indiscernible due to the improved stability after ageing. Initially, the trend of the OCP mainly varies between −0.2 V and −0.5 V with large amplitude transients. At a later stage, the OCP settles at a relatively stable value of −0.4 V (shown in Fig. 8**a**). The large OCP variation at the beginning is probably caused by the competition between local penetration of water and chloride ions and re-passivation. It has been reported that LDH layers can act as chloride ion sorbent according to their anion exchange capabilities, which impairs the potential damage by chloride ions at the start of re-immersion [65,66]. In this work, several representative timeframes are analysed after the OCP becomes relatively stable. The original signals are schematically displayed at the background of the Hilbert spectra with their relative amplitudes in Fig. 8**b** to Fig. 8**e**. At the beginning, two parallel electrochemical reactions with typical electrochemical responses, i.e. fingerprints, at intermediate frequencies (0.01–0.1 Hz) and low frequencies (< 0.01 Hz) are present in the HHT spectrum. With the passing of the re-immersion time, the frequencies of the dominant reactions gradually move towards the intermediate frequency range, indicating that the time span of most transients becomes shorter over the course of the measurement. Based on the characterization results that the duration of S-phase-related corrosion from initiation to undercutting (i.e. loss of the related galvanic S-phase-to-matrix coupling) is typically shorter than that of the large constituent particles, it can be inferred that the low-frequency transients that appear in the signal shown in Fig. 8**b** are mainly related to the corrosion activity surrounding the S-phase particles, whereas the intermediate-frequency transients are generated by corrosion attack related to large constituent phases. It can therefore be assumed that corrosion activity related to the S-phase particles is typically a lower-frequency process than corrosion related to large constituent phase particles, although the latter may last longer upon re-immersion. Figs. 8**c** and 8**d** show the transition from reactions dominated by S-phase-related corrosion to constituent phase-related corrosion, since S-phase-related corrosion shows a higher activity and experiences undercutting from the matrix at an earlier stage (after approximately 8 h). In Fig. 8**e**, the relative energy contribution from S-phase-related corrosion is almost negligible. The EN results point out that S-phase- and large constituent phase-related corrosion activities occur almost simultaneously, albeit that the corrosion activities at and around constituent phases last longer.

3.5. Schematic corrosion model for the lithium-based conversion layer

Current findings and previous work [57,62] in relation to the characterization of the corrosion behaviour of the lithium-based conversion layer during re-immersion are pivotal in proposing a more detailed corrosion mechanism to explain spatiotemporally resolved local degradation events. Fig. 9 proposes a corrosion mechanism of the freshly formed conversion layer at the aluminium matrix during re-immersion. Immediately after re-immersion, the trapped lithium carbonate is released from the conversion layer due to the instability of the structure when it is exposed to a lithium-free liquid environment [64]. The released lithium carbonate can create a local alkaline environment that favours a continuous formation of the lithium-based conversion layer. Simultaneously, due to the loss of lithium and carbonate ions, the crystal structure of the top Li/Al LDH layer gradually collapses. The inner dense layer undergoes a loss of lithium carbonate as well, which decreases its integrity. This suggests that the entire conversion layer matures insufficiently when removed from the lithium-containing solution immediately.

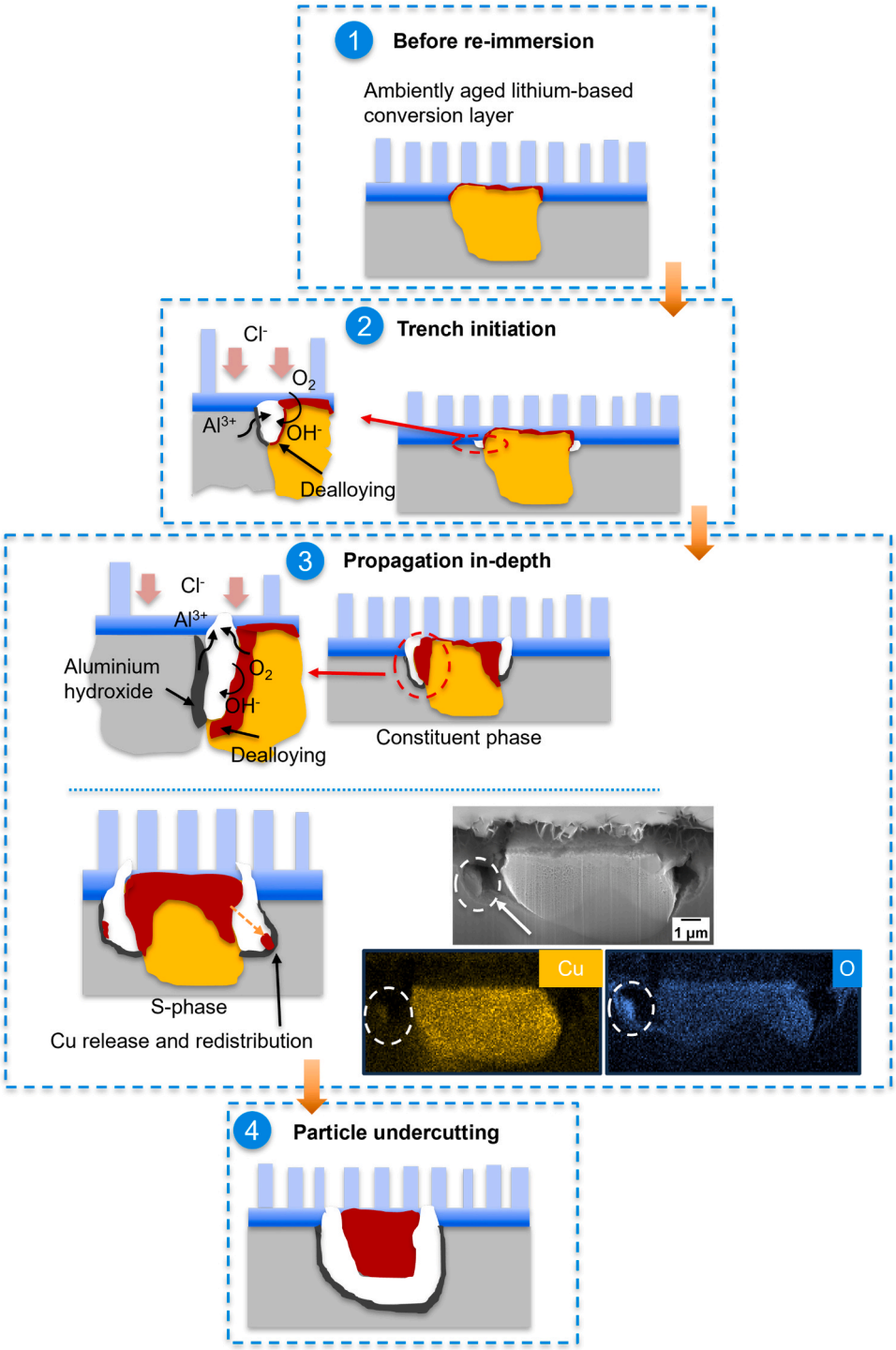

Fig. 10. Schematic overview of the localized corrosion mechanism at and around S- and constituent phase particles under the 36 h ambiently-aged lithium-based conversion layer during re-immersion. The insert in step 3 is a cross-sectional SEM micrograph with EDX results showing released copper from a dealloyed S-phase particle, redeposited locally at the trench wall.

Based on previous studies focused on dealloying-driven localized corrosion involving the IMPs in AA2024-T3, the localized corrosion at and around IMPs under the protection of the lithium-based conversion layer can be divided into several stages [38,60]. These include trench initiation, depth propagation and particle undercutting, as described in Fig. 10 [38,60]. IMPs are more prone to corrosion attack due to insufficient coverage of the inner dense layer, especially for the large constituent particles. For the case of the S-phase, although its relatively small size facilitates its coverage by the incomplete inner layer, this is still insufficient to fully suppress its high chemical instability, since chloride ions can penetrate the conversion layer during re-immersion. Another issue is the fact that the S-phase undergoes significant and rapid dealloying during the conversion layer formation process, leading to a copper enrichment that acts as strong cathodic areas [36]. At the early stages of re-immersion, considering the different electrochemical properties between the aluminium matrix and IMPs, trenching is more likely to occur at the interface between the matrix and the IMPs. At this stage, chloride ions and water gradually reach the bottom of the

conversion layer, promoting the dissolution of the aluminium matrix and dealloying of the IMPs which make IMPs more prone to serve as cathodic zones. With the ongoing corrosion process underneath the conversion layer and the accumulation of corrosion products, the breakdown of the conversion layer commences. This process allows enhanced interaction of the corroding region with the external environment. Both the S- and constituent phases endure dealloying. The S-phase undergoes a selective dissolution of aluminium and magnesium, whereas the constituent phase particles experience the dissolution of manganese, aluminium and iron to a small extent [38]. Dealloying generates a local aggregation of remnant copper and/or iron establishing nano-galvanic coupling which drives the anodic dissolution of the rest of the particle and the adjacent aluminium matrix. At this stage, the dealloying of the IMPs and in-depth propagation of the trenches occur simultaneously, however the S-phase exhibits faster dealloying kinetics and establishes a stronger galvanic effect with the adjacent matrix than the large constituent phase [67]. Moreover, local degradation of the dealloying of the S-phase might occur and contribute to the release and redistribution of copper ions to nearby regions [60]. This phenomenon can greatly enhance the further dissolution of the nearby aluminium matrix and make the corrosion area to increase in size around the S-phase [60]. Finally, the local dissolution of the aluminium matrix around IMPs continues until the detachment of the IMPs. For constituent particles, this process takes into account a longer time. For this reason, this is less likely to occur within 12 h of re-immersion under conditions of the current study. After undercutting, the corroding IMPs acquire a higher corrosion potential and become fully dealloyed and may undergo further self-corrosion [60]. The undercutting also blocks the galvanic relationship between the matrix and the IMPs, resulting in a milder environment due to the significantly reduced oxygen reduction reaction and reduced production of H^+ caused by the hydrolysis of metal ions. This is beneficial for the stabilization of aluminium hydroxide corrosion products which gradually cover the aluminium matrix and isolate the matrix further from the external corrosive environment.

4. Conclusions

Top-view and cross-sectional characterization of the lithium-based conversion layer grown on AA2024-T3 before re-immersion reveal that the aluminium matrix is covered by a complete bilayer conversion coating (a top columnar layer as well as an inner dense layer), yet the formation of the inner layer is incomplete over the IMPs. Although this deficient inner layer is able to cover small IMPs, it fails to develop over large constituent particles. This is caused by the relatively high electrochemical stability of these large particles, as well as by the fact that the conversion layer formation over constituent phases relies on the lateral propagation of aluminate ions derived from the adjacent aluminium matrix. During re-immersion in a NaCl solution, the freshly formed lithium-based conversion layer undergoes a gradual dissolution over the entire conversion layer which is triggered by its chemical instability. This makes the aluminium matrix underneath the conversion layer more prone to corrosion attack, although initially some trapped lithium carbonate is released which can inhibit the corrosion to a certain extent. In the case of the ambiently-aged sample, after re-immersion dealloying and trenching are more likely to occur at and around the S- and large constituent phase particles. Large constituent phase-related corrosion occurs due to the lower conversion layer quality locally, whereas S-phase-related corrosion can be attributed to the highly active nature of the S-phase and a greater extent of dealloying during the conversion layer formation, leading to increased copper enrichment at the surface of the S-phase. The galvanic couples between the aluminium matrix and the IMPs can be triggered when water and chloride ions reach the bottom of the conversion layer. Ongoing corrosion reactions allow the trench to propagate along the interface between the matrix and the IMPs until the particles are fully undercut. Simultaneously, the IMPs also undergo gradual dealloying, albeit the S-phase at a faster pace and exhibiting higher trench propagation kinetics as compared to the large constituent phase.

CRediT authorship contribution statement

Arjan Mol: Writing – review & editing, Supervision, Conceptualization. **Peter Visser:** Writing – review & editing. **Yaiza Gonzalez-Garcia:** Writing – review & editing, Supervision, Conceptualization. **Ziyu Li:** Writing – original draft, Methodology, Investigation, Formal analysis, Data curation, Conceptualization. **Axel Homborg:** Writing – review & editing, Supervision, Conceptualization.

Declaration of Competing Interest

The authors declare that they have no known competing financial interests or personal relationships that could have appeared to influence the work reported in this paper.

Data Availability

Data will be made available on request.

Acknowledgements

The authors wish to acknowledge the financial support from the China Scholarship Council (CSC).

Appendix A. Supporting information

Supplementary data associated with this article can be found in the online version at doi:10.1016/j.corsci.2024.112061.

References

[1] N.L. Sukiman, X. Zhou, N. Birbilis, A.E. Hughes, J.M.C. Mol, S. J, X. Zhou, G. E, Durability and Corrosion of Aluminium and Its Alloys: Overview, Property Space, Techniques and Developments, in: Z. Ahmad (Ed.), Aluminium Alloys - New Trends in Fabrication and Applications, InTech, 2012. https://doi.org/10.5772/53752.
[2] A.E. Hughes, C. MacRae, N. Wilson, A. Torpy, T.H. Muster, A.M. Glenn, Sheet AA2024-T3: a new investigation of microstructure and composition, Surf. Interface Anal. 42 (2010) 334–338, https://doi.org/10.1002/sia.3163.
[3] A. Boag, A.E. Hughes, N.C. Wilson, A. Torpy, C.M. MacRae, A.M. Glenn, T. H. Muster, How complex is the microstructure of AA2024-T3? Corros. Sci. 51 (2009) 1565–1568, https://doi.org/10.1016/j.corsci.2009.05.001.
[4] A.E. Hughes, N. Birbilis, J.M.C. Mol, S.J. Garcia, X. Zhou, G.E. Thompson, High Strength Al-Alloys: Microstructure, Corrosion and Principles of Protection, in: Z. Ahmad (Ed.), Recent Trends in Processing and Degradation of Aluminium Alloys, InTech, 2011. https://doi.org/10.5772/18766.
[5] S.J. Andersen, C.D. Marioara, J. Friis, S. Wenner, R. Holmestad, Precipitates in aluminium alloys, Adv. Phys.: X 3 (2018) 1479984, https://doi.org/10.1080/23746149.2018.1479984.
[6] C. Blanc, B. Lavelle, G. Mankowski, The role of precipitates enriched with copper on the susceptibility to pitting corrosion of the 2024 aluminium alloy, Corros. Sci. 39 (1997) 495–510, https://doi.org/10.1016/S0010-938X(97)86099-4.
[7] N. Birbilis, Y.M. Zhu, S.K. Kairy, M.A. Glenn, J.-F. Nie, A.J. Morton, Y. Gonzalez-Garcia, H. Terryn, J.M.C. Mol, A.E. Hughes, A closer look at constituent induced localised corrosion in Al-Cu-Mg alloys, Corros. Sci. 113 (2016) 160–171, https://doi.org/10.1016/j.corsci.2016.10.018.
[8] P. Campestrini, H. Terryn, J. Vereecken, J.H.W. de Wit, Chromate Conversion Coating on Aluminum Alloys: III. Corrosion Protection, J. Electrochem. Soc. 151 (2004) B370, https://doi.org/10.1149/1.1736683.
[9] M.W. Kendig, R.G. Buchheit, Corrosion Inhibition of Aluminum and Aluminum Alloys by Soluble Chromates, Chromate Coatings, and Chromate-Free Coatings, CORROSION 59 (2003) 379–400, https://doi.org/10.5006/1.3277570.
[10] G.O. Ilevbare, J.R. Scully, J. Yuan, R.G. Kelly, Inhibition of Pitting Corrosion on Aluminum Alloy 2024-T3: Effect of Soluble Chromate Additions vs Chromate Conversion Coating, CORROSION 56 (2000) 227–242, https://doi.org/10.5006/1.3287648.
[11] A.E. Hughes, R.J. Taylor, B.R.W. Hinton, Chromate Conversion Coatings on 2024 Al Alloy, Surf. Interface Anal. 25 (1997) 223–234, https://doi.org/10.1002/(SICI)1096-9918(199704)25:4<223::AID-SIA225>3.0.CO;2-D.
[12] R. Saha, R. Nandi, B. Saha, Sources and toxicity of hexavalent chromium, J. Coord. Chem. 64 (2011) 1782–1806, https://doi.org/10.1080/00958972.2011.583646.
[13] M. Becker, Chromate-free chemical conversion coatings for aluminum alloys, Corros. Rev. 37 (2019) 321–342, https://doi.org/10.1515/corrrev-2019-0032.

[14] I. Milošev, G.S. Frankel, Review—Conversion Coatings Based on Zirconium and/or Titanium, J. Electrochem. Soc. 165 (2018) C127, https://doi.org/10.1149/2.0371803jes.

[15] O. Gharbi, S. Thomas, C. Smith, N. Birbilis, Chromate replacement: what does the future hold? Npj Mater. Degrad. 2 (2018) 12, https://doi.org/10.1038/s41529-018-0034-5.

[16] R.L. Twite, G.P. Bierwagen, Review of alternatives to chromate for corrosion protection of aluminum aerospace alloys, Prog. Org. Coat. 33 (1998) 91–100, https://doi.org/10.1016/S0300-9440(98)00015-0.

[17] Y. Guo, G.S. Frankel, Characterization of trivalent chromium process coating on AA2024-T3, Surf. Coat. Technol. 206 (2012) 3895–3902, https://doi.org/10.1016/j.surfcoat.2012.03.046.

[18] L. Li, G.M. Swain, Effects of aging temperature and time on the corrosion protection provided by trivalent chromium process coatings on AA2024-T3, ACS Appl. Mater. Interfaces 5 (2013) 7923–7930, https://doi.org/10.1021/am4020023.

[19] P. Santa Coloma, U. Izagirre, Y. Belaustegi, J.B. Jorcin, F.J. Cano, N. Lapeña, Chromium-free conversion coatings based on inorganic salts (Zr/Ti/Mn/Mo) for aluminum alloys used in aircraft applications, Appl. Surf. Sci. 345 (2015) 24–35, https://doi.org/10.1016/j.apsusc.2015.02.179.

[20] O. Lopez-Garrity, G.S. Frankel, Corrosion inhibition of aluminum alloy 2024-T3 by sodium molybdate, J. Electrochem. Soc. 161 (2013) C95, https://doi.org/10.1149/2.044403jes.

[21] D.S. Kharitonov, J. Sommertune, C. Örnek, J. Ryl, I.I. Kurilo, P.M. Claesson, J. Pan, Corrosion inhibition of aluminium alloy AA6063-T5 by vanadates: local surface chemical events elucidated by confocal Raman micro-spectroscopy, Corros. Sci. 148 (2019) 237–250, https://doi.org/10.1016/j.corsci.2018.12.011.

[22] V. Moutarlier, M.P. Gigandet, B. Normand, J. Pagetti, EIS characterisation of anodic films formed on 2024 aluminium alloy, in sulphuric acid containing molybdate or permanganate species, Corros. Sci. 47 (2005) 937–951, https://doi.org/10.1016/j.corsci.2004.06.019.

[23] A.K. Mishra, R. Balasubramaniam, Corrosion inhibition of aluminum alloy AA 2014 by rare earth chlorides, Corros. Sci. 49 (2007) 1027–1044, https://doi.org/10.1016/j.corsci.2006.06.026.

[24] K.A. Yasakau, M.L. Zheludkevich, S.V. Lamaka, M.G.S. Ferreira, Mechanism of corrosion inhibition of AA2024 by rare-earth compounds, J. Phys. Chem. B 110 (2006) 5515–5528, https://doi.org/10.1021/jp0560664.

[25] R.G. Buchheit, G.E. Stoner, Chromate-free corrosion resistant talc coatings for aluminum alloys, Sandia National Labs., Albuquerque, NM (United States), 1992. ⟨https://www.osti.gov/biblio/6725477⟩.

[26] P. Visser, H. Terryn, J.M.C. Mol, On the importance of irreversibility of corrosion inhibitors for active coating protection of AA2024-T3, Corros. Sci. 140 (2018) 272–285, https://doi.org/10.1016/j.corsci.2018.05.037.

[27] P. Visser, Y. Liu, H. Terryn, J.M.C. Mol, Lithium salts as leachable corrosion inhibitors and potential replacement for hexavalent chromium in organic coatings for the protection of aluminum alloys, J. Coat. Technol. Res. 13 (2016) 557–566, https://doi.org/10.1007/s11998-016-9784-6.

[28] C.A. Drewien, M.O. Eatough, D.R. Tallant, C.R. Hills, R.G. Buchheit, Lithium-aluminum-carbonate-hydroxide hydrate coatings on aluminum alloys: Composition, structure, and processing bath chemistry, J. Mater. Res. 11 (1996) 1507–1513, https://doi.org/10.1557/JMR.1996.0188.

[29] R.G. Buchheit, M.D. Bode, G.E. Stoner, Corrosion-resistant, chromate-free talc coatings for aluminum, Corrosion 50 (1994) 205–214, https://doi.org/10.5006/1.3293512.

[30] J. Gui, T.M. Devine, Influence of lithium on the corrosion of aluminum, Scr. Metall. 21 (6) (1987), https://doi.org/10.1016/0036-9748(87)90336-X.

[31] P. Visser, Y. Liu, X. Zhou, T. Hashimoto, G.E. Thompson, S.B. Lyon, L.G.J. van der Ven, A.J.M.C. Mol, H.A. Terryn, The corrosion protection of AA2024-T3 aluminium alloy by leaching of lithium-containing salts from organic coatings, Faraday Discuss. 180 (2015) 511–526, https://doi.org/10.1039/C4FD00237G.

[32] Y. Liu, P. Visser, X. Zhou, S.B. Lyon, T. Hashimoto, M. Curioni, A. Gholinia, G. E. Thompson, G. Smyth, S.R. Gibbon, D. Graham, J.M.C. Mol, H. Terryn, Protective film formation on AA2024-T3 aluminum alloy by leaching of lithium carbonate from an organic coating, J. Electrochem. Soc. 163 (2015) C45, https://doi.org/10.1149/2.0021603jes.

[33] Y. Liu, P. Visser, X. Zhou, S.B. Lyon, T. Hashimoto, A. Gholinia, G.E. Thompson, G. Smyth, S.R. Gibbon, D. Graham, J.M.C. Mol, H. Terryn, An investigation of the corrosion inhibitive layers generated from lithium oxalate-containing organic coating on AA2024-T3 aluminium alloy, Surf. Interface Anal. 48 (2016) 798–803, https://doi.org/10.1002/sia.5972.

[34] P. Visser, S.A. Hayes, Anti-corrosive coating composition, US8628689B2, 2014. ⟨https://patents.google.com/patent/US8628689B2/en⟩ (accessed January 3, 2024).

[35] P. Visser, A. Lutz, J.M.C. Mol, H. Terryn, Study of the formation of a protective layer in a defect from lithium-leaching organic coatings, Prog. Org. Coat. 99 (2016) 80–90, https://doi.org/10.1016/j.porgcoat.2016.04.028.

[36] A. Kosari, F. Tichelaar, P. Visser, H. Zandbergen, H. Terryn, J.M.C. Mol, Laterally-resolved formation mechanism of a lithium-based conversion layer at the matrix and intermetallic particles in aerospace aluminium alloys, Corros. Sci. 190 (2021) 109651, https://doi.org/10.1016/j.corsci.2021.109651.

[37] Z. Li, P. Visser, A.E. Hughes, A. Homborg, Y. Gonzalez-Garcia, A. Mol, Review of the state of art of Li-based inhibitors and coating technology for the corrosion protection of aluminium alloys, Surf. Coat. Technol. 478 (2024) 130441, https://doi.org/10.1016/j.surfcoat.2024.130441.

[38] A. Kosari, F. Tichelaar, P. Visser, H. Zandbergen, H. Terryn, J.M.C. Mol, Dealloying-driven local corrosion by intermetallic constituent particles and dispersoids in aerospace aluminium alloys, Corros. Sci. 177 (2020) 108947, https://doi.org/10.1016/j.corsci.2020.108947.

[39] J.R. Waldrop, M.W. Kendig, Nucleation of chromate conversion coating on aluminum 2024-T3 investigated by atomic force microscopy, J. Electrochem. Soc. 145 (1998) L11, https://doi.org/10.1149/1.1838199.

[40] P. Campestrini, H. Terryn, J. Vereecken, J.H.W. de Wit, Chromate conversion coating on aluminum alloys: II: effect of the microstructure, J. Electrochem. Soc. 151 (2004) B359, https://doi.org/10.1149/1.1736682.

[41] G. Šekularac, J. Kovač, I. Milošev, Comparison of the electrochemical behaviour and self-sealing of zirconium conversion coatings applied on aluminium alloys of series 1xxx to 7xxx, J. Electrochem. Soc. 167 (2020) 111506, https://doi.org/10.1149/1945-7111/aba875.

[42] P. Visser, Y. Gonzalez-Garcia, J.M.C. Mol, H. Terryn, Mechanism of passive layer formation on AA2024-T3 from alkaline lithium carbonate solutions in the presence of sodium chloride, J. Electrochem. Soc. 165 (2018) C60–C70, https://doi.org/10.1149/2.1011802jes.

[43] R.G. Buchheit, G.E. Stoner, Chromate-free corrosion resistant talc coatings for aluminum alloys, Sandia National Labs., Albuquerque, NM (United States), 1992. ⟨https://www.osti.gov/biblio/6725477⟩.

[44] R.G. Buchheit, Alkaline oxide conversion coatings for aluminum alloys, Sandia National Lab. (SNL-NM), Albuquerque, NM (United States), 1996. ⟨https://www.osti.gov/biblio/195749⟩.

[45] R.G. Buchheit, M.A. Martinez, C.B. Cooper, Corrosion resistant coatings for aluminum by hydrothermal film formation in alkaline Li-salt solutions, MRS Online Proc. Libr. 432 (1996) 273, https://doi.org/10.1557/PROC-432-273.

[46] A.M. Homborg, T. Tinga, X. Zhang, E.P.M. van Westing, P.J. Oonincx, J.H.W. de Wit, J.M.C. Mol, Time–frequency methods for trend removal in electrochemical noise data, Electrochim. Acta 70 (2012) 199–209, https://doi.org/10.1016/j.electacta.2012.03.062.

[47] Ł. Lentka, J. Smulko, Methods of trend removal in electrochemical noise data – Overview, Measurement 131 (2019) 569–581, https://doi.org/10.1016/j.measurement.2018.08.023.

[48] N.E. Huang, Z. Shen, S.R. Long, M.C. Wu, H.H. Shih, Q. Zheng, N.-C. Yen, C. C. Tung, H.H. Liu, The empirical mode decomposition and the Hilbert spectrum for nonlinear and non-stationary time series analysis, Proc. R. Soc. Lond. Ser. A: Math. Phys. Eng. Sci. 454 (1998) 903–995, https://doi.org/10.1098/rspa.1998.0193.

[49] P. Frank Pai, A.N. Palazotto, HHT-based nonlinear signal processing method for parametric and non-parametric identification of dynamical systems, Int. J. Mech. Sci. 50 (2008) 1619–1635, https://doi.org/10.1016/j.ijmecsci.2008.10.001.

[50] A.M. Homborg, E.P.M. van Westing, T. Tinga, X. Zhang, P.J. Oonincx, G.M. Ferrari, J.H.W. de Wit, J.M.C. Mol, Novel time–frequency characterization of electrochemical noise data in corrosion studies using Hilbert spectra, Corros. Sci. 66 (2013) 97–110, https://doi.org/10.1016/j.corsci.2012.09.007.

[51] N.A. Payne, L.I. Stephens, J. Mauzeroll, The Application of Scanning Electrochemical Microscopy to Corrosion Research, Corrosion 73 (2017) 759–780, https://doi.org/10.5006/2354.

[52] D. Polcari, P. Dauphin-Ducharme, J. Mauzeroll, Scanning Electrochemical Microscopy: A Comprehensive Review of Experimental Parameters from 1989 to 2015, Chem. Rev. 116 (2016) 13234–13278, https://doi.org/10.1021/acs.chemrev.6b00067.

[53] Z. Ye, Z. Zhu, Q. Zhang, X. Liu, J. Zhang, F. Cao, In situ SECM mapping of pitting corrosion in stainless steel using submicron Pt ultramicroelectrode and quantitative spatial resolution analysis, Corros. Sci. 143 (2018) 221–228, https://doi.org/10.1016/j.corsci.2018.08.014.

[54] C. Gabrielli, S. Joiret, M. Keddam, H. Perrot, N. Portail, P. Rousseau, V. Vivier, Development of a Coupled SECM-EQCM Technique for the Study of Pitting Corrosion on Iron, J. Electrochem. Soc. 153 (2006) B68, https://doi.org/10.1149/1.2161574.

[55] K. Mansikkamäki, P. Ahonen, G. Fabricius, L. Murtomäki, K. Kontturi, Inhibitive Effect of Benzotriazole on Copper Surfaces Studied by SECM, J. Electrochem. Soc. 152 (2004) B12, https://doi.org/10.1149/1.1829413.

[56] J.J. Santana, J. Izquierdo, R.M. Souto, Uses of scanning electrochemical microscopy (SECM) for the characterization with spatial and chemical resolution of thin surface layers and coating systems applied on metals: a review, Coatings 12 (2022) 637, https://doi.org/10.3390/coatings12050637.

[57] Z. Li, A. Homborg, Y. Gonzalez-Garcia, P. Visser, M. Soleimani, A. Mol, The effect of ambient ageing on the corrosion protective properties of a lithium-based conversion layer, J. Electrochem. Soc. 170 (2023) 031504, https://doi.org/10.1149/1945-7111/acc1a6.

[58] A. Kosari, F. Tichelaar, P. Visser, P. Taheri, H. Zandbergen, H. Terryn, J.M.C. Mol, Nanoscopic and in-situ cross-sectional observations of Li-based conversion coating formation using liquid-phase TEM, Npj Mater. Degrad. 5 (2021) 1–9, https://doi.org/10.1038/s41529-021-00189-y.

[59] A. Kosari, P. Visser, F. Tichelaar, S. Eswara, J.-N. Audinot, T. Wirtz, H. Zandbergen, H. Terryn, J.M.C. Mol, Cross-sectional characterization of the conversion layer formed on AA2024-T3 by a lithium-leaching coating, Appl. Surf. Sci. 512 (2020) 145665, https://doi.org/10.1016/j.apsusc.2020.145665.

[60] A. Kosari, H. Zandbergen, F. Tichelaar, P. Visser, P. Taheri, H. Terryn, J.M.C. Mol, In-situ nanoscopic observations of dealloying-driven local corrosion from surface initiation to in-depth propagation, Corros. Sci. 177 (2020) 108912, https://doi.org/10.1016/j.corsci.2020.108912.

[61] P. Visser, M. Meeusen, Y. Gonzalez-Garcia, H. Terryn, J.M.C. Mol, Electrochemical Evaluation of Corrosion Inhibiting Layers Formed in a Defect from Lithium-Leaching Organic Coatings, J. Electrochem. Soc. 164 (2017) C396, https://doi.org/10.1149/2.1411707jes.

[62] Z. Li, A. Homborg, Y. Gonzalez-Garcia, A. Kosari, P. Visser, A. Mol, Evaluation of the formation and protectiveness of a lithium-based conversion layer using electrochemical noise, Electrochim. Acta 426 (2022) 140733, https://doi.org/10.1016/j.electacta.2022.140733.
[63] L. Huang, J. Wang, Y. Gao, Y. Qiao, Q. Zheng, Z. Guo, Y. Zhao, D. O'Hare, Q. Wang, Synthesis of LiAl2-layered double hydroxides for CO2 capture over a wide temperature range, J. Mater. Chem. A 2 (2014) 18454–18462, https://doi.org/10.1039/C4TA04065A.
[64] K.A. Tarasov, V.P. Isupov, L.E. Chupakhina, D. O'Hare, A time resolved, in-situ X-ray diffraction study of the de-intercalation of anions and lithium cations from [LiAl2(OH)6]nX·qH2O (X = Cl−, Br−, NO3−, SO42−), J. Mater. Chem. 14 (2004) 1443–1447, https://doi.org/10.1039/B314473A.
[65] H.N. McMurray, G. Williams, Inhibition of Filiform Corrosion on Organic-Coated Aluminum Alloy by Hydrotalcite-Like Anion-Exchange Pigments, Corrosion 60 (2004) 219–228, https://doi.org/10.5006/1.3287724.
[66] Y. Su, S. Qiu, D. Yang, S. Liu, H. Zhao, L. Wang, Q. Xue, Active anti-corrosion of epoxy coating by nitrite ions intercalated MgAl LDH, J. Hazard. Mater. 391 (2020) 122215, https://doi.org/10.1016/j.jhazmat.2020.122215.
[67] S. Lebouil, J. Tardelli, E. Rocca, P. Volovitch, K. Ogle, Dealloying of Al2Cu, Al7Cu2Fe, and Al2CuMg intermetallic phases to form nanoparticulate copper films, Mater. Corros. 65 (2014) 416–424, https://doi.org/10.1002/maco.201307550.